High-Bandwidth Control of Nanopositioning Stages via an Inner-Loop Delayed Position Feedback

Mei-Ju Yang, *Student Member, IEEE*, Jin-Bo Niu, Chun-Xia Li, *Student Member, IEEE*, Guo-Ying Gu, *Member, IEEE*, and Li-Min Zhu, *Member, IEEE*

***Abstract*—This paper presents a novel high-bandwidth control approach for piezo-actuated nanopositioning stages. A delayed position feedback (DPF) controller is first developed in the inner loop to damp the resonant mode of piezo-actuated stages. A generalized Runge–Kutta method (GRKM) is proposed to determine the parameters of the DPF controller with pole placement. The benefit of the DPF for active damping is its simple structure and ease of implementation. Then, a high-gain proportional-integral (PI) controller is designed in the outer loop to deal with the hysteresis nonlinearity, disturbance and modeling errors. The stability of the control system is analyzed via a graphical method. Finally, experiments are conducted to demonstrate the effectiveness and superiority of the proposed approach in terms of tracking accuracy at high speed as compared to the PI controller.**

Note to Practitioners—**Piezo-actuated nanopositioning stages play an increasingly important role in the fields of scanning probe microscopy and micro/nano manipulation. They have the advantages of fast response, large force, and fine resolution. However, such stages inherently exhibit vibration and hysteresis behaviors that could cause oscillations and positioning errors. This study presents a two-degree-of-freedom high-bandwidth control approach, where the inner-loop delayed position feedback controller, determined by a generalized Runge-Kutta method, is designed to suppress the vibration effect, and the outer-loop high-gain PI controller is adopted to improve the tracking performance in the presence of hysteresis nonlinearity, disturbance and modeling errors. The effectiveness of the proposed control approach is demonstrated by experiments on a piezo-actuated nanopositioning stage. Due to the simple structure and ease of implementation, the developed control approach can be applied to other piezo-actuated systems as well.**

***Index Terms*—Delayed position feedback (DPF), high-bandwidth control, nanopositioning stages, piezoelectric actuators.**

Manuscript received January 15, 2015; revised April 23, 2015; accepted June 24, 2015. Date of publication July 22, 2015; date of current version October 02, 2015. This paper was recommended for publication by Associate Editor T. Kawahara and Editor Y. Sun upon evaluation of the reviewers' comments. This work was supported in part by the National Natural Science Foundation of China under under Grant 51325502 and Grant 51405293 and the Specialized Research Fund for the Doctoral Program of Higher Education under Grant 20130073110037.

The authors are with the State Key Laboratory of Mechanical System and Vibration, School of Mechanical Engineering, Shanghai Jiao Tong University, Shanghai 200240, China (e-mail: yangmeixianglian@sjtu.edu.cn; niujinbo@hotmail.com; lichunxia@sjtu.edu.cn; guguoying@sjtu.edu.cn; zhulm@sjtu.edu.cn).

Color versions of one or more of the figures in this paper are available online at http://ieeexplore.ieee.org.

Digital Object Identifier 10.1109/TASE.2015.2451368

I. Introduction

With the ability of generating three-dimensional images of material surfaces at nanometer resolution, atomic force microscopy (AFM) has been widely used in many applications [1], [2]. One of the key components of AFM is the nanopositioning stage, which is employed to move the sample in three directions [3], [4]. Most nanopositioning stages utilize piezoelectric actuators for actuation due to the excellent advantages of fast response, high positioning precision, and large stiffness. However, the nanopositioning stage suffers from two major issues that degrade its positioning performance [5]–[8]: 1) the inherent hysteresis nonlinearity of the piezoelectric material and 2) the highly resonant behavior due to the mechanical dynamics.

To compensate for the hysteresis nonlinearities, many control approaches have been reported [9]–[16]. Therein, feedback control with high gains is shown to be an effective method to reduce the hysteresis effect and achieve accurate tracking of references [15], [16]. However, the presence of lightly damped resonance imposes restrictions on gain margins, limiting the bandwidth of the controller and maximum SPM scan frequency to 1/100th to 1/10th of the first resonance frequency of the stages [17]. Damping of resonant peaks is an effective method to increase the bandwidth of the feedback control. Different damping techniques have been reported in the literature [18]–[23] such as positive position feedback, integral resonant control, and integral force feedback. Feedforward controllers [17], [24]–[26] such as inversion filters, input shaping techniques, and H_∞ feedforward control have also been reported to suppress the resonant peaks. However, feedforward controllers do not provide robustness to changes in system parameters which is critical in nanopositioning systems. A more comprehensive study on the control of nanopositioning stages can be found in [8] and [27].

Recently, the delayed position feedback (DPF) control scheme has re-attracted researchers' attention due to the advances in analysis of delayed differential equations. It has been widely used to reduce the unwanted vibrations in many applications [28]–[32] such as dynamic structures, flexible arms, and container cranes. The DPF control only employs a delayed position signal to achieve active damping of the resonance mode. The benefit is that, due to only one position sensor is required, the control scheme has a simple structure and ease of implementation. However, in this scheme, stability analysis is often complicated because of the introduction of time delay in the closed loop. In most cases, time delay is considered as a major source of instability, thus, many methods have been reported to investigate stability of time delay systems [33]. The most common method is the Padé approximation, which substitutes the exponential time-delay term in the characteristic equation with rational fraction. However, this simple approach has a limitation in accuracy, and at worst lead to instability of the system [34]. Other techniques such as the direct method (DM) [35], the Lambert W function [36], and the semi-discrezation method (SDM) [37], are known to be effective methods to investigate the stability of time-delay systems. Recently, a novel eigenvalue-based semi-analytical method, the generalized Runge–Kutta method (GRKM), was proposed in our previous research to predict the stability of milling systems [38], and extended to control the time-delay systems which was verified with high computational accuracy and efficiency [39]. However, no real-time applications of the GRKM were reported in the literature.

In this paper, we utilize the GRKM for high-bandwidth control of the piezo-actuated nanopositioning stages based on the time delay control. To the best of the authors' knowledge, this work is the first attempt at introducing the time delay control to the domain of high speed and high precision control of the piezo-actuated nanopositioning stages. The contributions of this work can be outlined as follows.

1) A DPF damping controller with a high-gain PI tracking controller is proposed and implemented on piezo-actuated stages to achieve the high-bandwidth tracking. The DPF control has the advantages of excellent damping performance, simple structure, and ease of implementation.
2) A GRKM is proposed for the pole placement of the plant with DPF control, resulting in a stable and damped closed-loop system. This approach was verified with high computational accuracy and efficiency for controlling the time delay systems.
3) The stability of the overall control system with time delay is analyzed by a graphical method, in which the stability boundary locus is plotted in the parameter plane.

The remainder of this paper is organized as follows. The experimental setup and system identification are described in Section II. In Section III, a high-bandwidth controller composed of a delayed position feedback controller and a high-gain PI controller is developed, and the stability analysis is performed. Section IV presents the experimental results to verify the effectiveness of the high-bandwidth controller, and the conclusion is given in Section V.

II. System Description and Identification

A. Experimental Setup

The experimental setup is shown in Fig. 1. The setup consists of a piezo-actuated stage, a dSPACE-DS1103 board, a high-voltage amplifier (HVA), and a position servo-control module (PSCM). The piezo-actuated stage is composed of an one-dimensional flexure hinge guiding mechanism, a preloaded piezoelectric stack actuator (PPSA), and a high-resolution strain gauge position sensor (SGPS). The PPSA (PSt 150/7/100 VS12, Piezomechanik, Germany) is used to drive the flexure

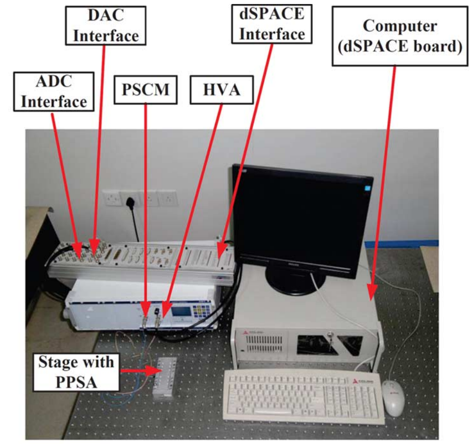

(a)

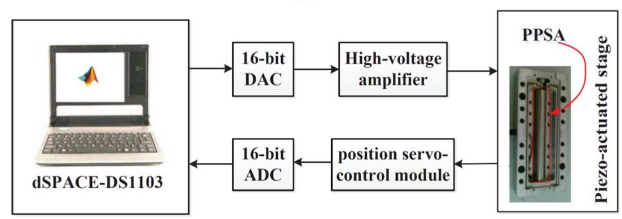

(b)

Fig. 1. Experimental setup of the piezo-actuated nanopositioning stage. (a) Experimental platform. (b) Block diagram.

mechanism with the maximum displacement of 75 μm. The SGPS integrated in the PPSA is used to measure the real-time displacement through the variance of the electrical resistance with the sensitivity of 0.148 V/μm and a resolution of 2.07 nm. The dSPACE-DS1103 board (Germany), equipped with 16-bit DAC and 16-bit ADC, is employed to implement the control algorithms in the Matlab/Simulink environment on the computer. The DAC board sends the signal generated by the computer to the amplifier, which provides excitation voltage to the PPSA in the range of 0–15 V. The ADC board is used to capture the real-time displacement data, which is changed into analogue voltage in the range of 0–10 V by the PSCM. The sampling frequency of the system is set to 20 kHz. The block diagram of the experiment setup is also shown in Fig. 1(b).

B. System Identification

To design a controller for the stages, the dynamic model of the piezo-actuated nanopositioning stage is required. To obtain the dynamic characteristic of the stage, a band-limited white noise signal with amplitude of 100 mV and frequency range of 0.05 Hz to 10 kHz is utilized to excite the stage. The dSPACE control system is utilized to simultaneously capture the excitation voltage and the corresponding measured displacement. It should be noted that the low amplitude of the input signal is intended to minimize the effect of the hysteresis nonlinearity. Therefore, the plant can be represented as a linear dynamic system. Then, the system identification toolbox of MATLAB is adopted to identify the dynamic model, which is expressed as

$$G(s) = \frac{592.8s^2 - 1.699 \times 10^7 s + 2.556 \times 10^{11}}{s^3 + 6662s^2 + 1.089 \times 10^8 s + 3.472 \times 10^{11}}. \quad (1)$$

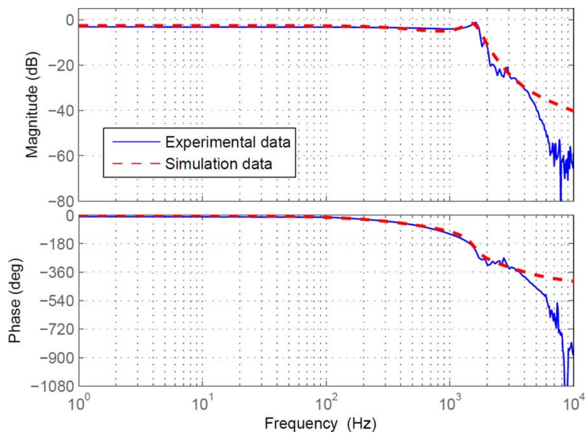

Fig. 2. Comparison of frequency responses of the experimental results and the simulation results of the identified model.

Fig. 2 shows the frequency responses of the experimental results and model simulation results. From the figure, it can be seen that in the frequency range of 1 to 4000 Hz, the identified model captures the dynamics of the system with sufficient accuracy. It should be noted that as the amplitude of the input increases, the effect of hysteresis is server which can cause significant positioning errors. In this work, the hysteresis is deemed as an input disturbance which can be mitigated by high-gain feedback control [15]. Therefore, the piezo-actuated stage is described by the linear dynamic model $G(s)$ together with a disturbance $d(t)$, where the hysteresis effect is involved in the unknown disturbance $d(t)$.

III. Controller Design

The control objective in high-bandwidth nanopositioning is to not only minimize the tracking error but also maximize the tracking speed of the nanopositioning stage. Analyzing the properties of the system model described in Section II, it can be observed that there is an obvious resonant mode, which will limit the tracking speed of the nanopositioning stage. In the following, a delayed position feedback (DPF) controller is firstly proposed to damp the system's resonant mode. Then, a high-gain PI tracking controller is utilized to achieve high-bandwidth nanopositioning.

A. Design of the DPF Controller

The DPF controller for a linear dynamic system is schematically shown in Fig. 3, where G is the dynamics model of the plant, d is the unknown disturbances, F represents the DPF controller, g is the feedback gain of the DPF, $e^{-s\tau}$ is the time delay term, $u(t)$ is the control input, $u_f(t)$ is the output of the DPF, and $y(t)$ is the output of the plant. It can be seen that the DPF possesses the excellent advantages of the simple structure. It only uses the signal $y(t)$ from a position sensor, and only has two design parameters. The critical feature of the DPF control is the utilization of a controlled time delay in the feedback loop. By adjusting the time delay τ and feedback gain g, one can achieve the pole placement of the closed-loop system in order to add active damping to the lightly damped stage.

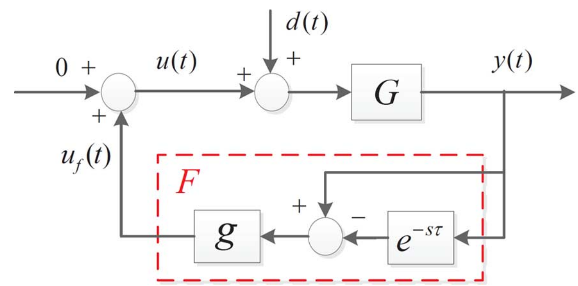

Fig. 3. Block diagram of the delayed position feedback control.

As shown in Fig. 3, the transfer function of the DPF can be written as

$$F(s) = g(1 - e^{-s\tau}). \tag{2}$$

Thus, the characteristic equation of the closed-loop system is deduced as

$$\Delta(s, \tau, g) = |1 - GF| = \left|1 - gG(1 - e^{-s\tau})\right| = 0. \tag{3}$$

Due to the exponential term, (3) is transcendental and results in an infinite number of characteristic roots. Thus, it is not feasible to specify all of the characteristic roots as the case of the systems without time delays. Furthermore, the classical pole placement methods for the systems without delays is no longer applicable. As an alternative, GRKM, an eigenvalue assignment method for the time delay systems, is proposed in our previous study [38], [39]. Pole placement is achieved by assigning the maximal eigenvalue obtained via the GRKM. In designing a control law for the time delay systems, it is crucial to handle the rightmost pole among the infinite number of ones. In this regard, the GRKM is very powerful. By adjusting the parameters of the DPF, i.e., the feedback gain g and time delay τ, we can assign the rightmost pole to the desired location. Therefore, the damping performance of the closed-loop system can be improved.

In order to implement the GRKM for pole placement in the nanopositioning stage, we rewrite the transfer function in (1) as

$$\begin{aligned} \dddot{y}(t) + a_2\ddot{y}(t) + a_1\dot{y}(t) + a_0 y(t) \\ = b_2\ddot{u}(t) + b_1\dot{u}(t) + b_0 u(t) \end{aligned} \tag{4}$$

where $a_2 = 6662$, $a_1 = 1.089 \times 10^8$, $a_0 = 3.472 \times 10^{11}$, $b_2 = 592.8$, $b_1 = -1.699 \times 10^7$, and $b_0 = 2.556 \times 10^{11}$.

The control signal $u(t)$ is calculated based on the DPF controller shown in Fig. 3, which is expressed as

$$u(t) = u_f(t) = g(y(t) - y(t - \tau)). \tag{5}$$

Substituting (5) into (4) yields

$$\begin{aligned} \dddot{y}(t) &+ (a_2 - gb_2)\ddot{y}(t) + (a_1 - gb_1)\dot{y}(t) \\ &+ (a_0 - gb_0)y(t) + gb_2\ddot{y}(t - \tau) \\ &+ gb_1\dot{y}(t - \tau) + gb_0 y(t - \tau) = 0. \end{aligned} \tag{6}$$

Defining a new vector $\boldsymbol{x}(t) = (\, y(t) \quad \dot{y}(t) \quad \ddot{y}(t)\,)^T$, then the delay differential equation (DDE) (6) can be transformed into

$$\dot{\boldsymbol{x}}(t) = \boldsymbol{A}\boldsymbol{x}(t) + \boldsymbol{B}\boldsymbol{x}(t-\tau) \tag{7}$$

where

$$\boldsymbol{A} = \begin{pmatrix} 0 & 1 & 0 \\ 0 & 0 & 1 \\ -a_0 + gb_0 & -a_1 + gb_1 & -a_2 + gb_2 \end{pmatrix} \tag{8}$$

and

$$\boldsymbol{B} = \begin{pmatrix} 0 & 0 & 0 \\ 0 & 0 & 0 \\ -gb_0 & -gb_1 & -gb_2 \end{pmatrix}. \tag{9}$$

Based on the state space expression in (7), the GRKM is utilized to analyze the stability of the dynamic system in (6) from a discretizaiton point of view. The derivation of the GRKM is detailed in Appendix A. The Floquet transition matrix with the GRKM is deduced as

$$\boldsymbol{\Phi} = \boldsymbol{P}^{-1} \cdot \boldsymbol{Q} \tag{10}$$

where $\boldsymbol{P}^{-1}$ denotes the inverse of matrix $\boldsymbol{P}$, and m is the dicretization steps. The dimension of matrix $\boldsymbol{P}$ is the same with $\boldsymbol{Q}$, i.e., $(m+1) \times (m+1)$, thus the dimension of the Floquet transition matrix $\boldsymbol{\Phi}$ is also $(m+1) \times (m+1)$.

Define $\mu_i (1 \le i \le (m+1))$ as the eigenvalues of the Floquet transition martrix $\boldsymbol{\Phi}$. Then, the Floquet exponents are deduced as

$$\lambda_i = \frac{1}{\tau} \ln(\mu_i). \tag{11}$$

Among the $(m+1)$ Floquet exponents, the one with the maximum real part corresponds to the rightmost characteristic root, which is denoted as $\lambda_{\max} = \lambda_{i^*}$. The index i^* is defined as

$$i^* = \underset{1 \le i \le (m+1)}{\arg\max}\ real(\lambda_i). \tag{12}$$

The DPF controller is designed to place the rightmost characteristic root $\lambda_{\max}$ to a desired place of the left half plane. This design is achieved by an optimization. The objective function is chosen as

$$\begin{aligned} \min \quad f(\lambda_{\max}) = & (real(\lambda_{\max}) - real(\lambda_0))^2 \\ & + (imag(\lambda_{\max}) - imag(\lambda_0))^2 \end{aligned} \tag{13}$$

where λ_0 denotes the desired characteristic root, $real(\lambda_{\max})$ and $real(\lambda_0)$ denote the real part of $\lambda_{\max}$ and λ_0, respectively, and $imag(\lambda_{\max})$ and $imag(\lambda_0)$ denote the imaginary part of $\lambda_{\max}$ and λ_0, respectively.

Experiments were conducted on the nanopositioning stage to demonstrate the effectiveness of the proposed controller. Open-loop poles of the transfer function $G(s)$ are computed as

$$\begin{aligned} p_{1,2} = & -1.5575 \times 10^3 \pm j9.7699 \times 10^3 \\ p_3 = & -3.5472 \times 10^3. \end{aligned} \tag{14}$$

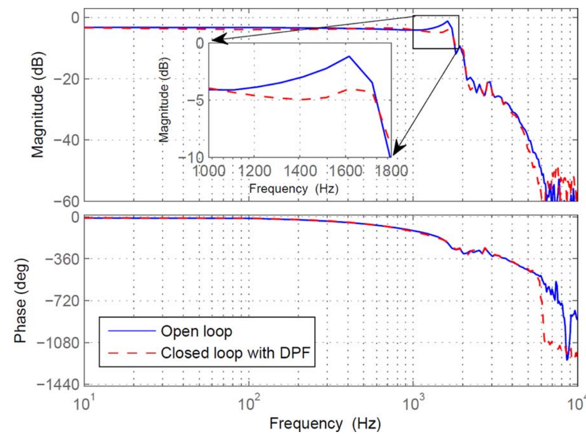

Fig. 4. Frequency response for systems with and without the DPF control.

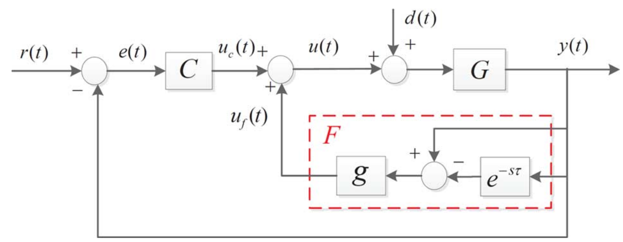

Fig. 5. Block diagram of the PI + DPF control.

In order to impart sufficient damping in the closed-loop system, the desired closed-loop pole locations should be set further into the left half plane. Here, we set the desired rightmost characteristic roots as

$$p'_{1,2} = -3.00 \times 10^3 \pm j9.7699 \times 10^3\,. \tag{15}$$

A particle swarm optimization method [40] is introduced to solve the optimization problem. The optimized parameters of the DPF controller are $\tau = 2.1721 \times 10^{-4}$, and $g = 0.3292$. Fig. 4 shows the frequency responses of the plant with and without the DPF controller. The frequency response with the DPF controller is presented by a red line. It is apparent from the figure that the resonance peak of the plant has been well damped by the DPF controller. Furthermore, it can be observed that the DPF control has no detrimental effect on the frequency responses over the resonance frequency. Therefore, the damping performance of the system has been improved significantly by the DPF control.

B. High-Gain Feedback Controller

To minimize the tracking errors of the piezo-actuated stage, a feedback controller is necessary in the control logic. Owing to the damping imparted by the DPF control, a proportional-integral (PI) controller C with high gains is implemented in the feedback loop, which is illustrated in Fig. 5 with $C = k_p + k_i/s$. The main drawback is the existence of the time delay in the closed loop, which may results in the instability. Thus, the stability of the closed-loop system is analyzed in the following via a graphical method [41], [42], in which the stability boundary locus is plotted in the parameter plane (k_p, k_i).

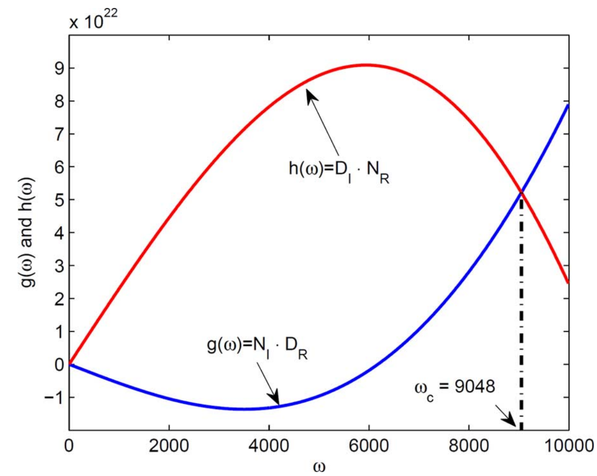

Fig. 6. Computation of the critical frequency ω_c.

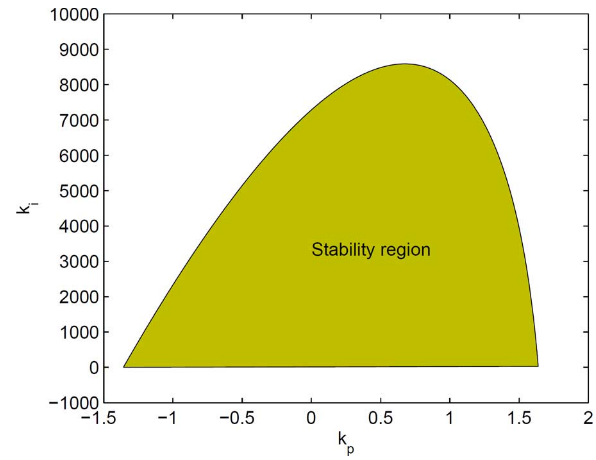

Fig. 7. Stability region of the closed-loop system.

From Fig. 5, we can obtain the characteristic polynomial of the closed-loop system, which is expressed as

$$\Delta(s) = 1 + G(s)C(s) - G(s)F(s). \tag{16}$$

Letting $s = j\omega$ and solving the equation $\Delta(j\omega) = 0$, we obtain

$$k_p = \frac{b_1\omega X + (b_2\omega^2 - b_0)Y}{-\omega[(b_2\omega^2 - b_0)^2 + b_1^2\omega^2]} \tag{17}$$

$$k_i = \frac{(b_2\omega^2 - b_0)\omega X - b_1\omega^2 Y}{-\omega[(b_2\omega^2 - b_0)^2 + b_1^2\omega^2]} \tag{18}$$

where X and Y are defined in (50). The derivation of k_p and k_i is detailed in Appendix B.

By letting ω vary from zero to ∞, a stability boundary locus for common roots of (17) and (18) can be plotted in the parameter plane (k_p, k_i). However, one can consider the frequency below the critical frequency ω_c or the ultimate frequency since the controller operates in this frequency range. Thus, the critical frequency can be used to obtain the stability boundary locus over a possible smaller range of frequency such as $\omega \in [0, \omega_c]$ [42]. Substituting $s = j\omega$ into the plant $P(s) = G(s)/(1 - G(s)F(s))$ gives

$$P(j\omega) = \frac{N_R + jN_I}{D_R + jD_I} \tag{19}$$

where N_R, N_I, D_R, and D_I are given in Appendix C. Since the phase of $P(s)$ at $s = j\omega_c$ is equal to $-180°$, we can get

$$\arctan\frac{N_I}{N_R} - \arctan\frac{D_I}{D_R} = -\pi \tag{20}$$

or

$$N_I D_R - D_I N_R = 0. \tag{21}$$

Thus, ω_c is the solution of (21). The plots of functions $g(\omega) = N_I D_R$ and $h(\omega) = D_I N_R$ versus ω are shown in Fig. 6, where it can be seen that the intersection point gives the value of ω_c. Therefore, the region enclosed by the stability boundary locus for $\omega \in [0, \omega_c]$ and $k_i = 0$ is the stability region which is the shaded region shown in Fig. 7.

In order to plot the stability region for specified gain and phase margin, a gain-phase margin tester $G_c = Ae^{-j\phi}$ [41] is connected in the feedforward path. Here, A is the gain margin of the system if $\phi = 0$, and ϕ is the phase margin of the system if $A = 1$. The closed-loop characteristic polynomial with the gain-phase margin tester will be

$$\Delta(j\omega) = 1 + Ae^{-j\phi}C(j\omega)P(j\omega). \tag{22}$$

Solving the equation $\Delta(j\omega) = 0$, it can be found that

$$k_p = \frac{b_1\omega M + (b_2\omega^2 - b_0)N}{-\omega A[(b_2\omega^2 - b_0)^2 + b_1^2\omega^2]} \tag{23}$$

$$k_i = \frac{(b_2\omega^2 - b_0)\omega M - b_1\omega^2 N}{-\omega A[(b_2\omega^2 - b_0)^2 + b_1^2\omega^2]} \tag{24}$$

with

$$\begin{aligned} M &= X\cos\phi - Y\sin\phi \\ N &= X\sin\phi + Y\cos\phi. \end{aligned} \tag{25}$$

Setting $A = 2$ and $\phi = 0$ in (23) and (24), the stability boundary locus for gain margin of 2 (6 dB) is plotted in Fig. 8, which is indicated by the blue line. Setting $A = 1$ and $\phi = 60°$ in (23) and (24), the stability boundary locus for phase margin of $60°$ is plotted by the red line. Thus, the region enclosed by these two stability boundary locus is the stability region, in which the gain margin is greater than 6 dB and the phase margin is greater than $60°$. The proportional and integral gains are respectively selected as 0.3 and 2800, which are tuned by the trial and error method in the stability region. The operating point is shown in Fig. 8.

IV. Experimental Results

Here, the aforementioned control strategy will be implemented for verification using the experimental setup shown in Fig. 1.

A. Bandwidth Test

Bandwidth is an important characteristic for a positioning system. It defines how fast a system response to the input signal is. The crossover frequency at -3 dB of the complementary sensitivity transfer function is commonly used as a measurement of bandwidth. In the experiment, a band-limit white noise signal is used to test the bandwidth of the developed PI and PI + DPF

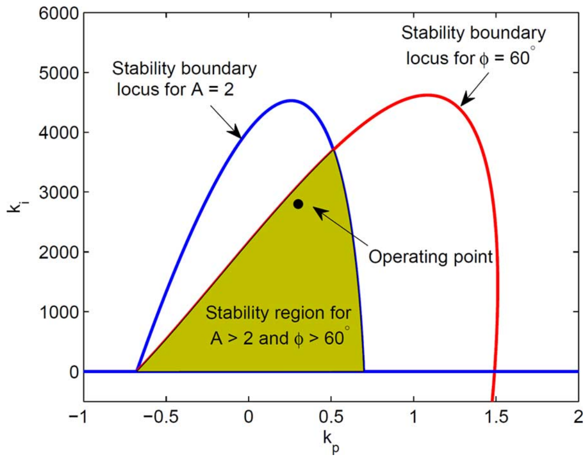

Fig. 8. Stability region of the closed-loop system for specified gain and phase margins.

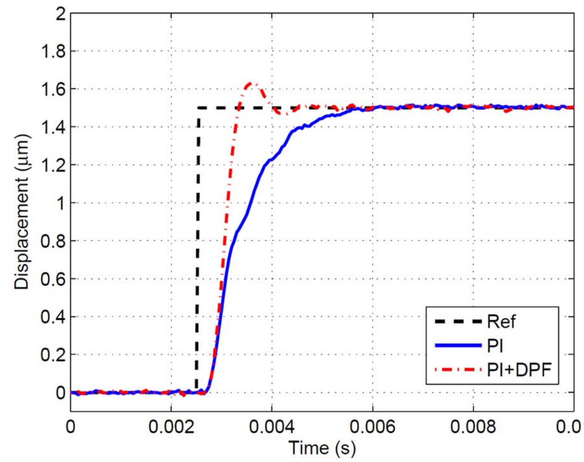

Fig. 10. Step responses of the PI and PI + DPF controllers.

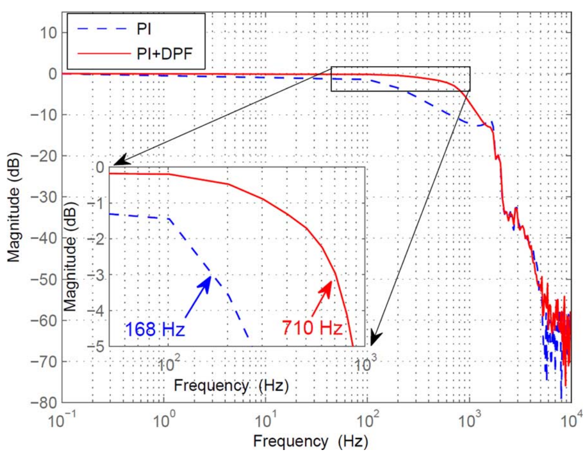

Fig. 9. Bandwidth measurement of the PI and PI + DPF controllers.

controllers. The control gains $k_p = 0.3$ and $k_i = 1500$ for the PI control are determined by the trial-and-error method to obtain a satisfied tracking performance, while $k_p = 0.3$ and $k_i = 2800$ are utilized for the PI+DPF control, as described in Section III. The magnitude plot of the closed-loop systems with PI and PI+DPF control are shown in Fig. 9. It can be seen that the crossover frequency with the PI + DPF control is 710 Hz, while the one with PI control is 168 Hz. The results demonstrate that with the PI + DPF control, the bandwidth of the system is increased by 4.23 times compared with the PI control.

In addition, the responses to the 1.5-μm step input with the PI and PI + DPF controllers are shown in Fig. 10, using the same control gains k_p and k_i as those in the bandwidth test. It can be observed that under PI control, the output exhibits slight oscillations, and converges slowly with a 1.5-ms rising time and 2.91-ms settling time. In contrast, with the PI + DPF control, the output converges quickly with a 0.84-ms rising time and 1.80-ms settling time. These results clearly demonstrate the effectiveness of the PI + DPF control in terms of the speed.

B. Trajectory Tracking

Here, the triangular trajectories with fundamental frequencies from 1 to 250 Hz are used to evaluate the tracking performance of the proposed control method. First, a performance index is chosen for a quantitative comparison. When discussing the tracking performance in SPM applications, perfectly delayed tracking is better than imperfect timely tracking if we know the delay well. According to the reference [43], the following two performance indexes shall be used in this work for the comparative study:

$$e_m = \frac{\max\limits_{t\in[0,T)} |y(t) - r(t - k^* T_s)|}{\max(r(t)) - \min(r(t))} \times 100\% \tag{26}$$

$$e_{rms} = \frac{\sqrt{\frac{1}{T}\int\limits_0^T (y(t) - r(t - k^* T_s))^2\, dt}}{\max(r(t)) - \min(r(t))} \times 100\% \tag{27}$$

where e_m and e_{rms} represent the maximum error and the root mean square error, respectively, T is the period of the reference signal, $T_s = 50$ μs is the controller sampling period, $y(t)$ is the actual position, $r(t)$ is the desired reference, $r(t - k^* T_s)$ is the shifted reference, and the variable k^* is defined as

$$k^* = \arg\min_k \max_{t\in[0,NT)} |y(t) - r(t - kT_s)| \tag{28}$$

where k is a variable defined on $[0, \quad T/T_s]$.

As an illustration, Fig. 11 shows a comparison of the tracking performance with PI and PI + DPF control for a 100-Hz triangular wave. The blue dashed lines indicate the reference position, the red solid lines represent the actual position, while the black dashed–dotted line denotes the shifted reference. The difference between the reference and the shifted reference is only a time delay. From the figure, it can be seen that the tracking performance of PI + DPF control is significantly better than PI control. This is further evidenced in Fig. 12, which shows comparisons of tracking errors with PI and PI + DPF control under triangular trajectories with different input frequencies. It should be noted that the tracking-lag is not included in the error calculation as this can be eliminated in practical applications by a phase-lead in either the applied reference, or the recorded data [22]. If real-time elimination of tracking-lag is required, an additional feedforward controller can be adopted [17], [25].

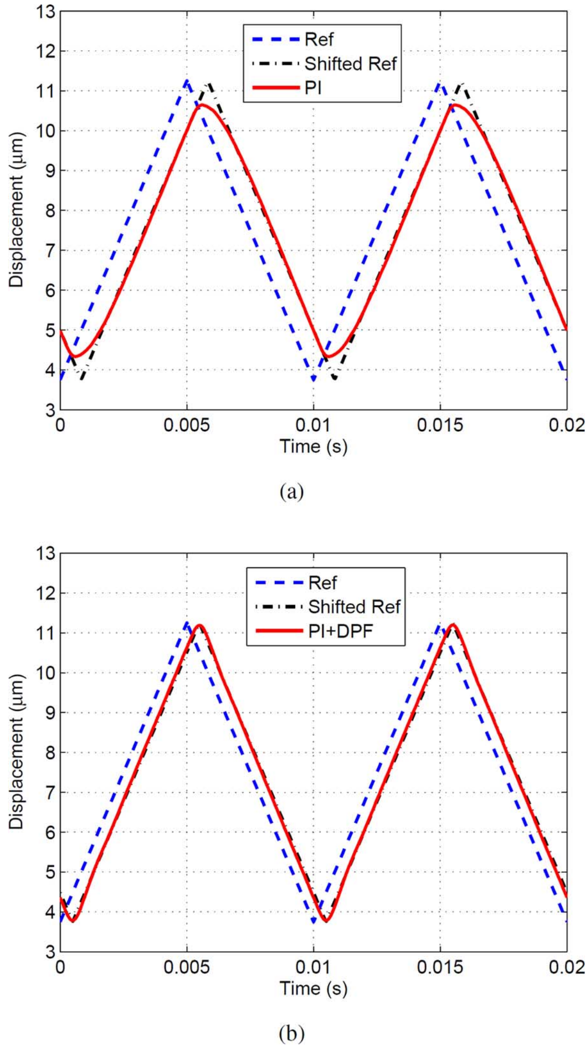

Fig. 11. Tracking results of the PI and PI + DPF controllers under a 100-Hz triangular trajectory.

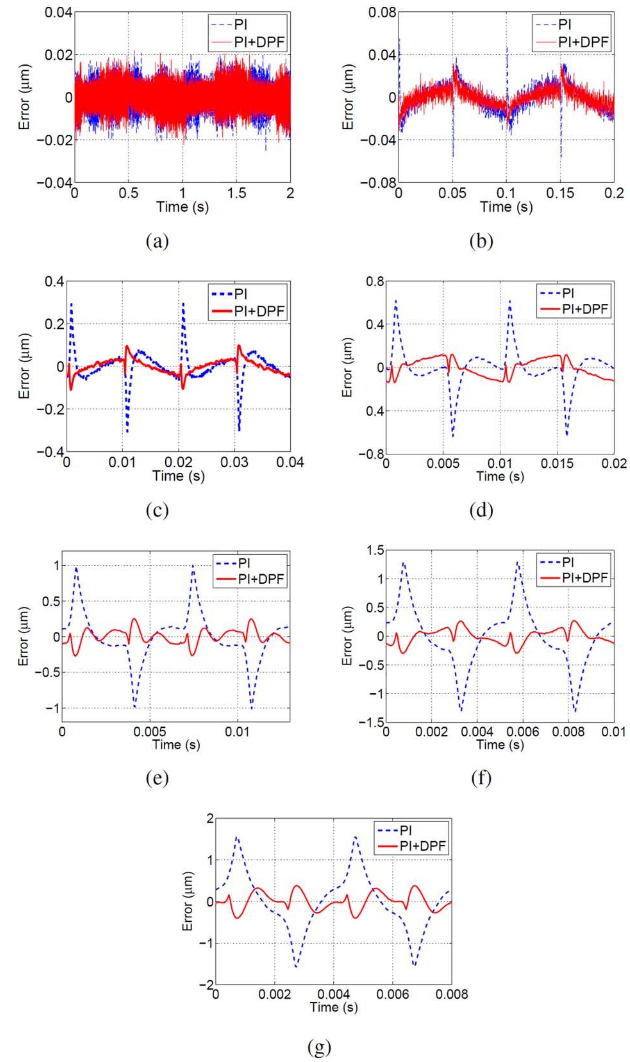

Fig. 12. Comparison of tracking errors of the PI and PI + DPF controllers under triangular trajectories with fundamental frequencies of (a) 1 Hz, (b) 10 Hz, (c) 50 Hz, (d) 100 Hz, (e) 150 Hz, (f) 200 Hz, and (g) 250 Hz.

From Fig. 12, it can be found that, with the increase of input frequencies, the tracking performance of the PI control is severely degraded, while the PI + DPF control exhibits a much better performance. For a quantitative comparison, Table I shows the tracking errors of the PI and PI + DPF controllers under the triangular trajectories with different frequencies. It can be observed that the maximum error e_m and the root mean square error e_{rms} of the PI + DPF control are reduced by 78.30% and 55.13%, respectively, as compared with those of the PI control at 100 Hz. It is known that a triangular waveform can be well approximated by its first four odd harmonics (i.e., first, third, fifth, and seventh). The bandwidth of the closed-loop system with the PI + DPF control is 710 Hz. Thus, the piezo-actuated nanopositioning stage with this controller can accurately track triangular trajectory up to 100 Hz, and its tracking performance would degrade severely when the input frequency is higher. These theoretic results are verified by the experimental results shown in Fig. 12 and Table I. It can be seen that, as the input frequencies increase, the tracking errors of the PI + DPF control slowly increase.

TABLE I
TRACKING ERRORS OF THE PI AND PI + DPF CONTROLLERS UNDER TRIANGULAR TRAJECTORIES WITH DIFFERENT FUNDAMENTAL FREQUENCIES

Frequency	PI		PI+DPF	
(Hz)	$e_m(\%)$	$e_{rms}(\%)$	$e_m(\%)$	$e_{rms}(\%)$
1	0.3406	0.0601	0.2969	0.0575
10	0.7507	0.1611	0.4243	0.1090
50	4.0800	0.8660	1.4775	0.4446
100	8.5363	2.4035	1.8523	1.0785
150	13.5687	4.6840	3.6390	1.3693
200	17.4473	7.1954	4.0195	1.6943
250	20.9133	9.4206	5.3809	2.7007

When the input frequencies are below 100 Hz, the e_m and e_{rms} of the PI + DPF control remain below 1.86% and 1.08% and exceed 2% and 1%, respectively, as the input frequencies are over 100 Hz. Hence, it can be concluded that, with the PI + DPF control, the piezo-actuated nanopositioning stage can accurately track triangular trajectory up to 100 Hz.

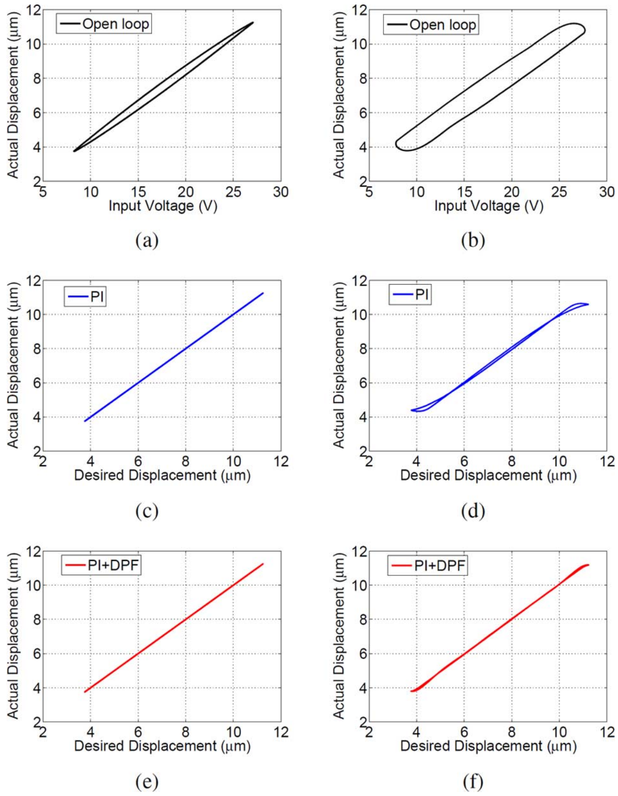

Fig. 13. Hysteresis compensation results at 1 Hz and 100 Hz triangular excitation with different control strategies: (a), (b) open-loop case; (c), (d) PI control; (e), (f) PI + DPF control.

TABLE II
HYSTERESIS EFFECT COMPENSATION WITH DIFFERENT CONTROL STRATEGIES

Frequency (Hz)	Width of hysteresis loop (%)		
	Open-loop	PI	PI+DPF
1	7.9267	0.3048	0.2741
100	21.7859	3.6391	1.4249

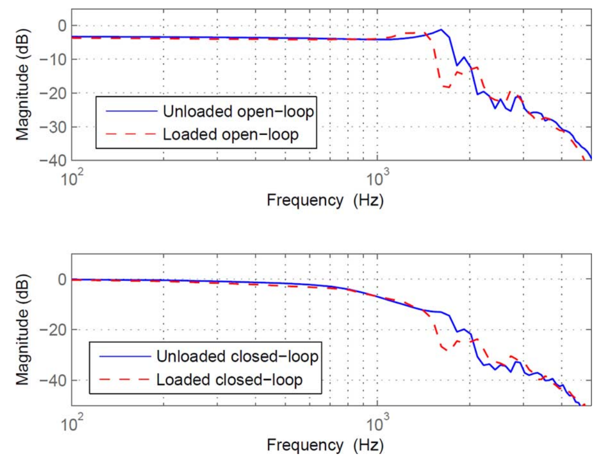

Fig. 14. Open-loop and closed-loop magnitude frequency responses from $r(t)$ to $y(t)$ with variation in resonance frequency.

C. Reduction of Hysteresis

To demonstrate the effectiveness of the hysteresis reduction using the proposed control approach, an experiment is performed in this section. In Fig. 13(a) and (b), the hysteresis effect of the stage at open-loop case is presented for the 1- and 100-Hz triangular trajectories, respectively, and are compared with the results of PI control [see Fig. 13(c) and (d)], and PI + DPF control [see Fig. 13(e) and (f)]. The reduction of hysteresis effect using the PI + DPF control over the open-loop case and the PI control is tabulated in Table II. The hysteresis effect is measured by the hysteresis width, which is defined as $((h/H \times 100\%)$, where h denotes the maximum width in the hysteresis loop along the vertical axis, and H defined in the form of $\max(y) - \min(y)$. In the case of 100 Hz, the width of the hysteresis loop is about 1.4249% using the PI + DPF control, 21.7859% using the open-loop control, and 3.6391% using the PI control. The reduction of the hysteresis effect using the PI + DPF control is about 93.46% and 60.84% in comparison to the open loop and the PI control, respectively. The results demonstrate the effectiveness of the proposed PI + DPF control against the hysteresis effect.

D. Robustness Test

Here, the robustness of the developed PI + DPF control is test under variation in resonance frequency. For the platform described in Fig. 1, the resonance frequency is 1616 Hz when unloaded. With a commonly used load, the resonance frequency reduces to 1415 Hz. The open-loop frequency responses under these two conditions are plotted in Fig. 14. The closed-loop frequency responses with the same PI + DPF controller are also shown in Fig. 14. From the figure, it can be seen that the proposed controller remains stable and provides good performance. The bandwidth of the closed-loop system is reduced from 710 to 552 Hz when the platform is loaded. Simulation test indicates that as the resonance frequency decreases, the bandwidth of the closed-loop system slowly degrades. The lowest allowable resonance frequency to keep the system stable is 1000 Hz.

V. CONCLUSION

In this paper, a high-bandwidth control method for piezo-actuated nanopositioning stages is proposed. The control structure is composed of two nested feedback loops. In the inner loop, the delayed position feedback controller is proposed to damp the resonant mode of the dynamic system. To realize the pole placement of the inner-loop system, a generalized Runge–Kutta method is utilized to calculate the rightmost characteristic root by constructing the Floquet transition matrix. Then, an optimization is used to place the rightmost characteristic root to the desired place in the left half plane to impart sufficient damping in the closed-loop system. The outer loop is a high-gain PI tracking controller, which is used to maximize the closed-loop bandwidth and reduce the errors caused by the dynamics and nonlinearities. The stability of the overall control system is analyzed and discussed by a graphical method, in which the stability boundary locus is plotted in the parameter plane. The gain margin and phase margin can be obtained from the stability boundary locus. Finally, experiments are performed on a piezo-actuated nanopositioning stage to verify the effectiveness of the proposed control method. Compared with the standard PI tracking controller, the combination of PI and DPF controller achieved an increase in the closed-loop bandwidth from 168 to 710 Hz, a reduction in hysteresis effect by 60.84% at the case of 100 Hz and an improvement in triangular tracking by 78.30% in terms of the maximum error.

APPENDIX A

The Floquet transition matrix $\boldsymbol{\Phi}$ in (10) for the system in (7) using the GRKM was developed in our previous study [38], [39]. Here, we briefly summarize the derivation of the Floquet transition matrix.

First, in order to approximate the DDE with a series of ODEs, the time delay τ should be equally divided into m intervals. The span of each interval is written as h, i.e., $\tau = mh$. Based on the Volterra integral equation of the second kind, the analytical solution of (7) is deduced as

$$\boldsymbol{x}(t) = e^{\boldsymbol{A}(t-t_0)}\boldsymbol{x}(t_0) + \int_{t_0}^{t} [e^{\boldsymbol{A}(t-\xi)}\boldsymbol{B}\boldsymbol{x}(\xi-\tau)]d\xi \tag{29}$$

where $\boldsymbol{x}(t_0)$ denotes the initial value at starting time t_0. On arbitrary interval $[t_i, t_{i+1}]$ $(i = 0, 1, \ldots, m-1)$, we have

$$\boldsymbol{x}(t) = e^{\boldsymbol{A}(t-t_i)}\boldsymbol{x}(t_i) + \int_{t_i}^{t} [e^{\boldsymbol{A}(t-\xi)}\boldsymbol{B}\boldsymbol{x}(\xi-\tau)]d\xi. \tag{30}$$

To simplify the derivation process, the following symbols are introduced:

$$\boldsymbol{g}(t, t_i) = e^{\boldsymbol{A}(t-t_i)}\boldsymbol{x}(t_i) \tag{31}$$

and

$$\boldsymbol{L}(t, \xi, x(\xi)) = e^{\boldsymbol{A}(t-\xi)}\boldsymbol{B}\boldsymbol{x}(\xi-\tau). \tag{32}$$

Suppose the initial value is $\boldsymbol{x}_{2i}(i = 0, 1, \ldots, i_m)$, where i_m is an integer regarding the discretization number m

$$i_m = ceil(\frac{m}{2}) - 1 \tag{33}$$

where $ceil$ is a function that rounds positive numbers to plus infinity (e.g., $ceil(3.1) = 4$).

If $\boldsymbol{x}_{2i+1}$ is known, $\boldsymbol{x}_{2i+2}$ can be obtained with the Simpson's rule on $[t_{2i}, t_{2i+2}]$ as

$$\begin{aligned}\boldsymbol{x}_{2i+2} =& \boldsymbol{g}(t_{2i+2}, t_{2i}) + \frac{h}{3}\{\boldsymbol{L}(t_{2i+2}, t_{2i}, \boldsymbol{x}_{2i}) \\ &+ 4\boldsymbol{L}(t_{2i+2}, t_{2i+1}, \boldsymbol{x}_{2i+1}) \\ &+ \boldsymbol{L}(t_{2i+2}, t_{2i+2}, \boldsymbol{x}_{2i+2})\}.\end{aligned} \tag{34}$$

By introducing the middle point value $\boldsymbol{x}_{2i+1/2}$, $\boldsymbol{x}_{2i+1}$ is calculated with the classical fourth-order Runge-Kutta method

$$\begin{aligned}\boldsymbol{x}_{2i+1} =& \boldsymbol{g}(t_{2i+1}, t_{2i}) + \frac{h}{6}\{\boldsymbol{L}(t_{2i+1}, t_{2i}, \boldsymbol{x}_{2i}) \\ &+ 4\boldsymbol{L}(t_{2i+1}, t_{2i+1/2}, \boldsymbol{x}_{2i+1/2}) \\ &+ \boldsymbol{L}(t_{2i+1}, t_{2i+1}, \boldsymbol{x}_{2i+1})\}.\end{aligned} \tag{35}$$

Based on the barycentric three-point Lagrange interpolation formula, the middle point value $\boldsymbol{x}_{2i+1/2}$ is expressed as

$$\boldsymbol{x}_{2i+1/2} \approx \frac{3}{8}\boldsymbol{x}_{2i} + \frac{3}{4}\boldsymbol{x}_{2i+1} - \frac{1}{8}\boldsymbol{x}_{2i+2}. \tag{36}$$

Substituting (36) into (35) yields

$$\begin{aligned}\boldsymbol{x}_{2i+1} =& \boldsymbol{g}(t_{2i+1}, t_{2i}) + \frac{h}{6}\{\boldsymbol{L}(t_{2i+1}, t_{2i}, \boldsymbol{x}_{2i}) \\ &+ 4\boldsymbol{L}(t_{2i+1}, t_{2i+1/2}, \frac{3}{8}\boldsymbol{x}_{2i} + \frac{3}{4}\boldsymbol{x}_{2i+1} - \frac{1}{8}\boldsymbol{x}_{2i+2}) \\ &+ \boldsymbol{L}(t_{2i+1}, t_{2i+1}, \boldsymbol{x}_{2i+1})\}.\end{aligned} \tag{37}$$

Based on (34) and (37), the general iterative expressions (38) and (39) are obtained. Abbreviate $\boldsymbol{x}(t_{2i-\tau})$ as $\boldsymbol{x}_{2i-\tau}$ for conciseness. The odd term is written as

$$\begin{aligned}&\boldsymbol{F}_{2i}\boldsymbol{x}_{2i} + \boldsymbol{F}_{2i+1}\boldsymbol{x}_{2i+1} + \boldsymbol{F}_{2i+2}\boldsymbol{x}_{2i+2} \\ &= \boldsymbol{F}_{2i-\tau}\boldsymbol{x}_{2i-\tau} + \boldsymbol{F}_{2i+1-\tau}\boldsymbol{x}_{2i+1-\tau} \\ &\quad + \boldsymbol{F}_{2i+2-\tau}\boldsymbol{x}_{2i+2-\tau}\end{aligned} \tag{38}$$

where $\boldsymbol{F}_{2i} = -e^{\boldsymbol{A}h}$, $\boldsymbol{F}_{2i+1} = \boldsymbol{I}, \boldsymbol{F}_{2i+2} = \boldsymbol{0}$, $\boldsymbol{F}_{2i-m} = h/6e^{\boldsymbol{A}h}\boldsymbol{B} + h/6 \cdot 4e^{\boldsymbol{A}h/2}\boldsymbol{B} \cdot 3/8$, $\boldsymbol{F}_{2i+1-m} = h/6 \cdot 4e^{\boldsymbol{A}h/2}\boldsymbol{B} \cdot 3/4 + h/6\boldsymbol{B}$, $\boldsymbol{F}_{2i+2-m} = h/6 \cdot 4e^{\boldsymbol{A}h/2}\boldsymbol{B} \cdot (-1/8)$.

The even term is written as

$$\begin{aligned}\boldsymbol{G}_{2i}\boldsymbol{x}_{2i} + &\boldsymbol{G}_{2i+1}\boldsymbol{x}_{2i+1} + \boldsymbol{G}_{2i+2}\boldsymbol{x}_{2i+2} \\ &= \boldsymbol{G}_{2i-\tau}\boldsymbol{x}_{2i-\tau} + \boldsymbol{G}_{2i+1-\tau}\boldsymbol{x}_{2i+1-\tau} \\ &\quad + \boldsymbol{G}_{2i+2-\tau}\boldsymbol{x}_{2i+2-\tau}\end{aligned} \tag{39}$$

where $\boldsymbol{G}_{2i} = -e^{\boldsymbol{A}\cdot 2h}$, $\boldsymbol{G}_{2i+1} = \boldsymbol{0}$, $\boldsymbol{G}_{2i+2} = \boldsymbol{I}$, $\boldsymbol{G}_{2i-m} = h/3e^{\boldsymbol{A}\cdot 2h}\boldsymbol{B}$, $\boldsymbol{G}_{2i+1-m} = h/3 \cdot 4e^{\boldsymbol{A}h}\boldsymbol{B}$, and $\boldsymbol{G}_{2i+2-m} = h/3\boldsymbol{B}$.

Based on (38) and (39), the expression of the discrete map (40), shown at the top of the following page, is obtained.

Then, according to (40), the Floquet transition matrix is deduced as

$$\boldsymbol{\Phi} = \boldsymbol{P}^{-1} \cdot \boldsymbol{Q} \tag{43}$$

where $\boldsymbol{P}^{-1}$ denotes the inverse of matrix $\boldsymbol{P}$. The dimension of matrix $\boldsymbol{P}$ is the same with $\boldsymbol{Q}$, i.e., $(m+1) \times (m+1)$, thus the dimension of the Floquet transition matrix $\boldsymbol{\Phi}$ is also $(m+1) \times (m+1)$.

APPENDIX B

The tracking gains k_p and k_i in (17) and (18) are derived here. Substituting G, C, F into (16), the characteristic polynomial can be written as

$$\begin{aligned}\Delta(s) =& s^4 + (a_2 + k_p b_2 - g b_2)s^3 + (a_1 + k_p b_1 + k_i b_2 \\ &- g b_1)s^2 + (a_0 + k_p b_0 + k_i b_1 - g b_0)s + k_i b_0 \\ &+ (g b_2 s^3 + g b_1 s^2 + g b_0 s)e^{-s\tau}.\end{aligned} \tag{44}$$

Letting $s = j\omega$, (44) becomes

$$\Delta(j\omega) = R_\Delta + jI_\Delta \tag{45}$$

where R_Δ and I_Δ are the real and imaginary parts of $\Delta(j\omega)$, respectively, which are expressed as

$$\begin{aligned}R_\Delta =& \omega^4 - (a_1 + k_p b_1 + k_i b_2 - g b_1)\omega^2 + k_i b_0 \\ &+ (-g b_2 \omega^3 + g b_0 \omega)\sin(\tau\omega) - g b_1 \omega^2 \cos(\tau\omega) \\ I_\Delta =& -(a_2 + k_p b_2 - g b_2)\omega^3 - (g b_2 \omega^3 - g b_0 \omega)\cos(\tau\omega) \\ &+ (a_0 + k_p b_0 + k_i b_1 - g b_0)\omega + g b_1 \omega^2 \sin(\tau\omega).\end{aligned} \tag{46}$$

$$
\begin{aligned}
&\boldsymbol{P}\left[\boldsymbol{x}_0{}^T \quad \boldsymbol{x}_1{}^T \quad \boldsymbol{x}_2{}^T \quad \boldsymbol{x}_3{}^T \quad \boldsymbol{x}_4{}^T \quad \cdots \quad \boldsymbol{x}_{2i_m+1}{}^T \quad \boldsymbol{x}_{2i_m+2}{}^T\right]^T \\
&= \boldsymbol{Q}\left[\boldsymbol{x}_{0-\tau}{}^T \quad \boldsymbol{x}_{1-\tau}{}^T \quad \boldsymbol{x}_{2-\tau}{}^T \quad \boldsymbol{x}_{3-\tau}{}^T \quad \boldsymbol{x}_{4-\tau}{}^T \quad \cdots \quad \boldsymbol{x}_{2i_m+1-\tau}{}^T \quad \boldsymbol{x}_{2i_m+2-\tau}{}^T\right]^T
\end{aligned} \tag{40}
$$

where

$$
\boldsymbol{P} = \begin{bmatrix}
\boldsymbol{I} & \boldsymbol{0} & \boldsymbol{0} & \boldsymbol{0} & \boldsymbol{0} & \cdots & \boldsymbol{0} & \boldsymbol{0} & \boldsymbol{0} \\
\boldsymbol{F}_0 & \boldsymbol{F}_1 & \boldsymbol{F}_2 & \boldsymbol{0} & \boldsymbol{0} & \cdots & \boldsymbol{0} & \boldsymbol{0} & \boldsymbol{0} \\
\boldsymbol{G}_0 & \boldsymbol{G}_1 & \boldsymbol{G}_2 & \boldsymbol{0} & \boldsymbol{0} & \dots & \boldsymbol{0} & \boldsymbol{0} & \boldsymbol{0} \\
\boldsymbol{0} & \boldsymbol{0} & \boldsymbol{F}_2 & \boldsymbol{F}_3 & \boldsymbol{F}_4 & \dots & \boldsymbol{0} & \boldsymbol{0} & \boldsymbol{0} \\
\boldsymbol{0} & \boldsymbol{0} & \boldsymbol{G}_2 & \boldsymbol{G}_3 & \boldsymbol{G}_4 & \cdots & \boldsymbol{0} & \boldsymbol{0} & \boldsymbol{0} \\
\vdots & \vdots & \vdots & \vdots & \vdots & \ddots & \vdots & \vdots & \vdots \\
\boldsymbol{0} & \boldsymbol{0} & \boldsymbol{0} & \boldsymbol{0} & \boldsymbol{0} & \cdots & \boldsymbol{F}_{2i_m} & \boldsymbol{F}_{2i_m+1} & \boldsymbol{F}_{2i_m+2} \\
\boldsymbol{0} & \boldsymbol{0} & \boldsymbol{0} & \boldsymbol{0} & \boldsymbol{0} & \cdots & \boldsymbol{G}_{2i_m} & \boldsymbol{G}_{2i_m+1} & \boldsymbol{G}_{2i_m+2}
\end{bmatrix} \tag{41}
$$

$$
\boldsymbol{Q} = \begin{bmatrix}
\boldsymbol{0} & \boldsymbol{0} & \boldsymbol{0} & \boldsymbol{0} & \boldsymbol{0} & \cdots & \boldsymbol{0} & \boldsymbol{0} & \boldsymbol{I} \\
\boldsymbol{F}_{0-\tau} & \boldsymbol{F}_{1-\tau} & \boldsymbol{F}_{2-\tau} & \boldsymbol{0} & \boldsymbol{0} & \cdots & \boldsymbol{0} & \boldsymbol{0} & \boldsymbol{0} \\
\boldsymbol{G}_{0-\tau} & \boldsymbol{G}_{1-\tau} & \boldsymbol{G}_{2-\tau} & \boldsymbol{0} & \boldsymbol{0} & \dots & \boldsymbol{0} & \boldsymbol{0} & \boldsymbol{0} \\
\boldsymbol{0} & \boldsymbol{0} & \boldsymbol{F}_{2-\tau} & \boldsymbol{F}_{3-\tau} & \boldsymbol{F}_{4-\tau} & \dots & \boldsymbol{0} & \boldsymbol{0} & \boldsymbol{0} \\
\boldsymbol{0} & \boldsymbol{0} & \boldsymbol{G}_{2-\tau} & \boldsymbol{G}_{3-\tau} & \boldsymbol{G}_{4-\tau} & \cdots & \boldsymbol{0} & \boldsymbol{0} & \boldsymbol{0} \\
\vdots & \vdots & \vdots & \vdots & \vdots & \ddots & \vdots & \vdots & \vdots \\
\boldsymbol{0} & \boldsymbol{0} & \boldsymbol{0} & \boldsymbol{0} & \boldsymbol{0} & \cdots & \boldsymbol{F}_{2i_m-\tau} & \boldsymbol{F}_{2i_m+1-\tau} & \boldsymbol{F}_{2i_m+2-\tau} \\
\boldsymbol{0} & \boldsymbol{0} & \boldsymbol{0} & \boldsymbol{0} & \boldsymbol{0} & \cdots & \boldsymbol{G}_{2i_m-\tau} & \boldsymbol{G}_{2i_m+1-\tau} & \boldsymbol{G}_{2i_m+2-\tau}
\end{bmatrix} \tag{42}
$$

Then, the equation $\Delta(j\omega) = 0$ is equivalent to the real and imaginary parts of $\Delta(j\omega)$ to zeros, i.e., $R_\Delta = 0$, $I_\Delta = 0$. Considering k_p and k_i as parameters, we have

$$
\begin{aligned}
&k_p(-b_1\omega^2) + k_i(-b_2\omega^2 + b_0) = gb_1\omega^2\cos(\tau\omega) \\
&\quad +(gb_2\omega^3 - gb_0\omega)\sin(\tau\omega) - \omega^4 + (a_1 - gb_1)\omega^2
\end{aligned} \tag{47}
$$

and

$$
\begin{aligned}
&k_p(-b_2\omega^3 + b_0\omega) + k_i(b_1\omega) = -gb_1\omega^2\sin(\tau\omega) \\
&+(gb_2\omega^3 - gb_0\omega)\cos(\tau\omega) + (a_2 - gb_2)\omega^3 - (a_0 - gb_0)\omega.
\end{aligned} \tag{48}
$$

Let

$$
\begin{aligned}
W(\omega) &= -b_1\omega^2 \\
R(\omega) &= -b_2\omega^2 + b_0 \\
S(\omega) &= -b_2\omega^3 + b_0\omega \\
U(\omega) &= b_1\omega
\end{aligned} \tag{49}
$$

and

$$
\begin{aligned}
X(\omega) &= gb_1\omega^2\cos(\tau\omega) + (gb_2\omega^3 - gb_0\omega)\sin(\tau\omega) \\
&\quad - \omega^4 + (a_1 - gb_1)\omega^2 \\
Y(\omega) &= -gb_1\omega^2\sin(\tau\omega) + (gb_2\omega^3 - gb_0\omega)\cos(\tau\omega) \\
&\quad + (a_2 - gb_2)\omega^3 - (a_0 - gb_0)\omega.
\end{aligned} \tag{50}
$$

Then, (47) and (48) can be written as

$$
\begin{aligned}
k_pQ(\omega) + k_iR(\omega) &= X(\omega) \\
k_pS(\omega) + k_iU(\omega) &= Y(\omega).
\end{aligned} \tag{51}
$$

From these equations, we can obtain

$$
k_p = \frac{X(\omega)U(\omega) - Y(\omega)R(\omega)}{W(\omega)U(\omega) - R(\omega)S(\omega)} \tag{52}
$$

$$
k_i = \frac{Y(\omega)W(\omega) - X(\omega)S(\omega)}{W(\omega)U(\omega) - R(\omega)S(\omega)}. \tag{53}
$$

Substituting (49) into (52) and (53), we can get

$$
k_p = \frac{b_1\omega X + (b_2\omega^2 - b_0)Y}{-\omega[(b_2\omega^2 - b_0)^2 + b_1^2\omega^2]} \tag{54}
$$

$$
k_i = \frac{(b_2\omega^2 - b_0)\omega X - b_1\omega^2 Y}{-\omega[(b_2\omega^2 - b_0)^2 + b_1^2\omega^2]}. \tag{55}
$$

Appendix C

The expressions of N_R, N_I, D_R and D_I are given as follows:

$$
N_R = -b_2\omega^2 + b_0 \tag{56}
$$

$$
N_I = b_1\omega \tag{57}
$$

$$
\begin{aligned}
D_R &= g(b_2\omega^2 - b_0)(1 - \cos(\tau\omega)) \\
&= +gb_1\omega\sin(\tau\omega) + (-a_2\omega^2 + a_0)
\end{aligned} \tag{58}
$$

$$
\begin{aligned}
D_I &= g(b_2\omega^2 - b_0)\sin(\tau\omega) + gb_1\omega\cos(\tau\omega)) \\
&= -gb_1\omega + (-\omega^3 + a_1\omega).
\end{aligned} \tag{59}
$$

References

[1] S. Salapaka and M. Salapaka, "Scanning probe microscopy," *IEEE Control Syst.*, vol. 28, no. 2, pp. 65–83, Feb. 2008.

[2] T. Ando, T. Uchihashi, and T. Fukuma, "High-speed atomic force microscopy for nano-visualization of dynamic biomolecular processes," *Prog. Surf. Sci.*, vol. 83, no. 7-9, pp. 337–437, 2008.

[3] Q. Xu, "Design and development of a flexure-based dual-stage nanopositioning system with minimum interference behavior," *IEEE Trans. Autom. Sci. Eng.*, vol. 9, no. 3, pp. 554–563, Jun. 2012.

[4] U. Bhagat, B. Shirinzadeh, Y. Tian, and D. Zhang, "Experimental analysis of laser interferometry-based robust motion tracking control of a flexure-based mechanism," *IEEE Trans. Autom. Sci. Eng.*, vol. 10, no. 2, pp. 267–275, Apr. 2013.

[5] D. Croft, G. Shed, and S. Devasia, "Creep, hysteresis, and vibration compensation for piezoactuators: atomic force microscopy application," *J. Dyn. Syst. Meas. Control*, vol. 123, pp. 35–43, 2001.

[6] Y. Qin, B. Shirinzadeh, Y. Tian, and D. Zhang, "Design issues in a decoupled XY stage: Static and dynamics modeling, hysteresis compensation, and tracking control," *Sens. Actuators A, Phys.*, vol. 194, pp. 95–105, 2013.

[7] M. Yang, G. Gu, and L. Zhu, "High-bandwidth tracking control of piezo-actuated nanopositioning stages using closed-loop input shaper," *Mechatronics*, vol. 24, pp. 724–733, 2014.
[8] A. Fleming and K. Leang, *Design, Modeling and Control of Nanopositioning Systems*. London, U.K.: Springer, 2014.
[9] G. Song, J. Zhao, X. Zhou, and J. Abreu-García, "Tracking control of a piezoceramic actuator with hysteresis compensation using inverse preisach model," *IEEE/ASME Trans. Mechatron.*, vol. 10, no. 2, pp. 198–209, Apr. 2005.
[10] Q. Xu, "Identification and compensation of piezoelectric hysteresis without modeling hysteresis inverse," *IEEE/ASME Trans. Ind. Electron.*, vol. 60, no. 9, pp. 3927–3937, 2013.
[11] G. Gu, M. Yang, and L. Zhu, "Real-time inverse hysteresis compensation of piezoelectric actuators with a modified prandtl-ishlinskii model," *Rev. Sci. Instrum.*, vol. 83, p. 065106, 2012.
[12] Z. Li, C. Su, and T. Chai, "Compensation of hysteresis nonlinearity in magnetostrictive actuators with inverse multiplicative structure for Preisach model," *IEEE Trans. Autom. Sci. Eng.*, vol. 11, no. 2, pp. 613–619, Apr. 2014.
[13] Q. Xu and Y. Li, "Dahl model-based hysteresis compensation and precise positioning control of an XY parallel micromanipulator with piezoelectric actuation," *J. Dyn. Syst. Meas. Control*, vol. 132, no. 4, p. 041011, 2010.
[14] A. Fleming and K. Leang, "Charge drives for scanning probe microscope positioning stages," *Ultramicroscopy*, vol. 108, pp. 1551–1557, 2008.
[15] K. Leang and S. Devasia, "Feedback-linearized inverse feedforward for creep, hysteresis, and vibration compensation in AFM piezoactuators," *IEEE Trans. Control Syst. Technol.*, vol. 15, no. 5, pp. 927–935, May 2007.
[16] X. Chen and T. Hisayam, "Adaptive sliding-mode position control for piezo-actuated stage," *IEEE Trans. Ind. Electron.*, vol. 55, no. 11, pp. 3927–3934, Nov. 2008.
[17] G. Clayton, S. Tien, K. Leang, Q. Zou, and S. Devasia, "A review of feedforward control approaches in nanopositioning for high-speed SPM," *J. Dyn. Syst. Meas. Control*, vol. 131, p. 061101, 2009.
[18] I. Mahmood and S. Moheimani, "Making a commercial atomic force microscope more accurate and faster using positive position feedback control," *Rev. Sci. Instrum.*, vol. 80, 2009, Art. ID 063705.
[19] B. Bhikkaji, M. Ratnam, A. Fleming, and S. O. R. Moheimani, "High-performance control of piezoelectric tube scanners," *IEEE Trans. Control Syst. Technol.*, vol. 15, no. 5, pp. 853–866, May 2007.
[20] A. Fleming, S. Aphale, and S. Moheimani, "A new method for robust damping and tracking control of scanning probe microscope positioning stages," *IEEE/ASME Trans. Nanotechnol.*, vol. 9, no. 4, pp. 438–448, Jul. 2010.
[21] A. Fleming, "Nanopositioning system with force feedback for high-performance tracking and vibration control," *IEEE/ASME Trans. Mechatron.*, vol. 15, no. 3, pp. 433–447, Jun. 2010.
[22] A. Fleming and K. Leang, "Integrated strain and force feedback for high-performance control of piezoelectric actuators," *Sens. Actuators A, Phys.*, vol. 161, pp. 256–265, 2010.
[23] A. Eielsen, M. Vagia, J. Gravdahl, and K. Pettersen, "Damping and tracking control schemes for nanopositioning," *IEEE/ASME Trans. Mechatroni.*, vol. 19, no. 2, pp. 432–444, Apr. 2014.
[24] M. Rakotondrabe, C. Clevy, and P. Lutz, "Complete open loop control of hysteretic, creeped, and oscillating piezoelectric cantilevers," *IEEE Trans. Autom. Sci. Eng.*, vol. 7, no. 3, pp. 440–450, Jul. 2010.
[25] M. Yang, C. Li, G. Gu, and L. Zhu, "Improving scanning speed of the AFMs with inversion-based feedforward control," in *Proc. 4th Int. Conf. Manip. Manuf. Meas. Nanoscale*, Taipei, Taiwan, Oct. 2014, Art. ID 7057301.
[26] G. Schitter and A. Stemmer, "Identification and open-loop tracking control of a piezoelectric tube scanner for high-speed scanning-probe microscopy," *IEEE Trans. Control Syst. Technol.*, vol. 12, no. 3, pp. 449–454, Mar. 2004.
[27] G. Gu, L. Zhu, C. Su, H. Ding, and S. Fatikow, "Modeling and control of piezo-actuated nanopositioning stages: a survey," *IEEE Trans. Autom. Sci. Eng.*, DOI: 10.1109/TASE.2014.2352364.
[28] N. Olgac and B. Holm-Hansen, "A novel active vibration absorption technique: delayed resonator," *J. Sound Vib.*, vol. 176, no. 1, pp. 93–104, 1994.
[29] N. Olgac, H. Elamali, M. Hosek, and M. Renzulli, "Active vibration control of distributed systems using delayed resonator with acceleration feedback," *J. Dyn. Syst. Meas. Control*, vol. 119, pp. 380–389, 1997.
[30] A. Jnifene, "Active vibration control of flexible structures using delayed position feedback," *Syst. Control Lett.*, vol. 56, pp. 215–222, 2007.
[31] K. Alhazza, A. Nayfeh, and M. Daqaq, "On utilizing delayed feedback for active-multimode vibration control of cantilever beams," *J. Sound Vib.*, vol. 319, pp. 735–752, 2009.
[32] Z. Masoud and A. Nayfeh, "Sway reduction on container cranes using delayed feedback controller," *Nonlinear Dyn.*, vol. 34, pp. 347–358, 2003.
[33] K. Gu and N. Iculescu, "Survey on recent results in the stability and control of time-delay systems," *J. Dyn. Syst. Meas. Control*, vol. 125, no. 2, pp. 158–165, 2003.
[34] G. Silva, A. Datta, and S. Bhattacharyya, "Controller design via Padé approximation can lead to instability," in *Proc. 40th IEEE Conf. Decis. Control*, Orlando, FL, USA, 2001, pp. 4377–4737.
[35] N. Olgac and R. Sipahi, "An exact method for the stability analysis of time-delayed linear time-inbariant(LTI) systems," *IEEE Trans Autom. Control*, vol. 47, no. 5, pp. 793–797, May 2002.
[36] S. Yi, P. Nelson, and A. Ulsoy, "Eigenvalue assignment via the Lambert W function for control of time-delay systems," *J. Vib. Control*, vol. 16, no. 7-8, pp. 961–982, 2010.
[37] J. Sheng, O. Elbeyli, and J. Sun, "Stability and optimal feedback control for time-delayed linear periodic systems," *AIAA J.*, vol. 42, no. 5, pp. 908–911, 2004.
[38] J. Niu, Y. Ding, L. Zhu, and H. Ding, "Runge-Kutta methods for a semi-analytical prediction of milling stability," *Nonlinear Dyn.*, vol. 76, no. 1, pp. 289–304, 2014.
[39] J. Niu, Y. Ding, L. Zhu, and H. Ding, "Eigenvalue assignment for control of time-delay systems via the generalized Runge-Kutta method," *J. Dyn. Syst. Meas. Control*, vol. 137, no. 5, 2015, Art. ID 091003.
[40] M. Yang, G. Gu, and L. Zhu, "Parameter identification of the generalized prandtl-ishlinskii model for piezoelectric actuators using modified particle swarm optimization," *Sens. Actuators A, Phys.*, vol. 189, pp. 254–265, 2013.
[41] K. Han and C. Chang, "Gain margins and phase margins for control systems with adjustable parameters," *J. Guidance Control Dyn.*, vol. 13, no. 3, pp. 404–408, 1990.
[42] N. Tan, I. Kaya, and D. Atherton, "A graphical method for computation of all stabilizing PI controllers," in *Proc. 16th IFAC World Congr.*, Prague, Czech Republic, 2005, vol. 16, pp. 349–354.
[43] J. Butterworth, L. Pao, and D. Abramovitch, "A discrete-time single-parameter combined feedforward/feedback adaptive-delay algorithm with applications to piezo-based raster tracking," *IEEE Trans. Control Syst. Technol.*, vol. 20, no. 2, pp. 416–423, Feb. 2012.

Mei-Ju Yang (S'12) received the B.E. degree in mechanical engineering from Shanghai Jiao Tong University, Shanghai, China, in 2009, where she is currently working toward the Ph.D. degree in mechanical engineering.

Her research interests include mechatronics, modeling, and control of nanopositioning stages.

Miss Yang was the recipient of the National Scholarship for Excellent Doctoral Student granted by Ministry of Education of China in 2013 and in 2014, respectively.

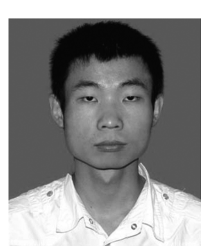

Jin-Bo Niu received the B.Sc. degree (with honors) in mechanical engineering from Dalian University of Technology, Dalian, China, in 2012. He is currently working toward the Ph.D. degree at Shanghai Jiao Tong University, Shanghai, China.

His research interest lies in mechanical manufacturing, machining dynamics, and vibration control.

Chun-Xia Li (S'12) received the B.E. degree (with honors) in mechanical engineering from Shanghai Jiao Tong University, Shanghai, China, in 2011, where she is currently working toward the Ph.D. degree in mechanical engineering.

Her research interests include compliant mechanisms and design and control of high-bandwidth nanopositioning stages.

Miss Li was the recipient of the National Scholarship for Excellent Master Student granted by Ministry of Education of China in 2012.

Guo-Ying Gu (S'10–M'13) received the B.E. degree (with honors) in electronic science and technology and Ph.D. degree (with honors) in mechatronic engineering from Shanghai Jiao Tong University, Shanghai, China, in 2006 and 2012, respectively.

From October 2010 to March 2011 and from November 2011 to March 2012, he was a Visiting Researcher with Concordia University, Montreal, QC, Canada. Since October 2012, he has been with Shanghai Jiao Tong University, Shanghai, China, where he is currently a Lecturer with the Faculty of the School of Mechanical Engineering. Supported by the Alexander von Humboldt Foundation, he was with the University of Oldenburg, Oldenburg, Germany, from August 2013 to July 2014. He has authored and coauthored more than 30 peer-reviewed papers, including 25 SCI-indexed journal papers. He has served as the guest editor of the special issue on Micro/Nano Mechatronics and Automation in *International Journal of Advanced Robotic Systems*. His research interests include robotics and equipment automation, design and high-bandwidth control of nanopositioning stages, modeling and control of systems involving with hysteresis.

Dr. Gu was the recipient of the Best Conference Paper Award of the 2011 IEEE International Conference on Information and Automation, Scholarship Award for Excellent Doctoral Student granted by Ministry of Education of China in 2011, Hiwin Excellent Mechanical Doctoral Dissertation Award of China in 2013, and Alexander von Humboldt Fellowship in 2013. He has served for several conferences as an international program committee member.

Li-Min Zhu (M'12) received the B.E. degree (with honors) and Ph.D. degree in mechanical engineering from Southeast University, Nanjing, China, in 1994 and 1999, respectively.

From November 1999 to January 2002, he was a Postdoctoral Fellow with Huazhong University of Science and Technology, Wuhan, China. Since March 2002, he has been with Shanghai Jiao Tong University, Shanghai, China. He is currently a a "Cheung Kong" Chair Professor, head of the Department of Mechanical and Automation Engineering, and vice director of the State Key Laboratory of Mechanical System and Vibration. His research interests include fixturing, CNC machining, and 3-D measurement of complex shaped parts and control, sensing, and instrumentation for micro/nano manufacturing. He has published one monograph and more than 180 peer-reviewed papers, including 105 on international journals.

Dr. Zhu was the recipient of the National Distinguished Youth Scientific Fund of China in 2013. Now he serves as an associate editor for the IEEE TRANSACTIONS ON AUTOMATION SCIENCE AND ENGINEERING and the Editorial Board Member of *Proceedings of the IMechE, Part B: Journal of Engineering Manufacture*.